Chapter

Ultimate Compressive Strength of Steel Stiffened-Plate Structures Triggered by Brittle Fracture under Cryogenic Conditions

Dong Hun Lee, Jeom Kee Paik, Jonas W. Ringsberg and P.J. Tan

Abstract

This chapter presents a practical method to investigate the effects of brittle fracture on the ultimate compressive strength of steel stiffened-plate structures under cryogenic conditions. Computational models are developed to analyse the ultimate compressive strength of steel stiffened-plate structures, triggered by brittle fracture, under cryogenic condition. A phenomenological form of the material model for the high-strength steel at cryogenic condition is proposed, that takes into account the Bauschinger effect, and implemented into a nonlinear finite element solver (LS-DYNA). Comparison between computational predictions and experimental measurements is made for the ultimate compressive strength response of a full-scale steel stiffened-plate structure, showing a good agreement between them.

Keywords: Bauschinger effect, brittle fracture, compressive strength, cryogenic condition, nonlinear finite element method, steel stiffened plate structure, ultimate strength

1. Introduction

Steel stiffened panels are used in naval, offshore, mechanical and civil engineering structures as their primary strength sub-structures. Occasionally, they are exposed to cryogenic conditions, e.g., due to the unwanted release of liquefied gas such as LNG (liquefied natural gas) or liquefied hydrogen as discussed in Paik et al. [1].

The ultimate strength is a primary criterion for the design of steel stiffened-plate structures [2–6], and it is essential to characterise the effects of cryogenic condition on the ultimate strength of such structures. The authors of this chapter have previously conducted collapse tests on full-scale steel stiffened-plate structures under axial-compressive loading at room temperature [1], at cryogenic condition [7] and at -80°C [8]. This chapter is part of a sequel to investigate the brittle fracture of steel stiffened-plate structures under cryogenic conditions. The tested structures were designed from a reference plate panel in an as-built containership carrying 1,900 TEU (twenty-foot equivalent units). They were fabricated at a shipyard using exactly the same welding technology as used in today's shipbuilding industry [9].

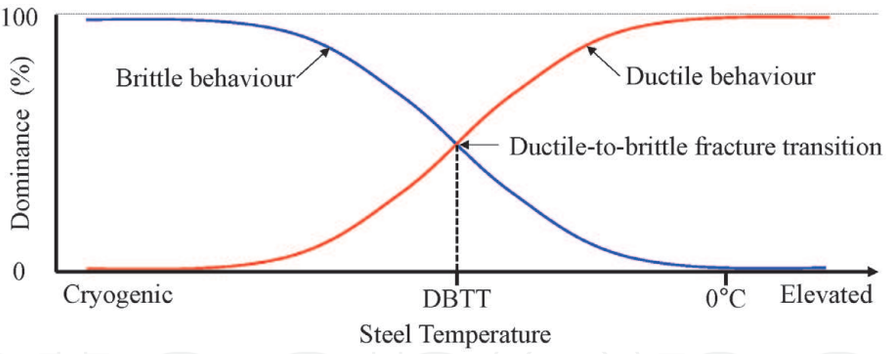

Figure 1.
Transition of the ductile-to-brittle behaviour for structural steel [5].

Structural fracture modes are classified into three groups [3, 4]: rupture, ductile fracture and brittle fracture. Material rupture occurs when failure occurs by cracking associated with necking localisation during large plastic flow. If the strain at which a material fractures is small, with very little ductility, it is a brittle fracture. An intermediate fracture mode between rupture and brittle fracture is called ductile fracture with partial ductility. Fracture behaviour of ductile materials such as carbon steels is quite different from that of inherently brittle materials. Ductile materials generally exhibit slow stable crack growth during crack extension, but they can show a similar behaviour to brittle materials at specific environments such as very low temperatures or lower than the ductile-to-brittle fracture transition temperatures (DBTT) and/or impact loading. It is also recognised that the Bauschinger effect of materials cannot be neglected at sub-zero temperatures and cryogenic condition as the material behaviour in compression is distinct from that in tension [3, 10, 11]. **Figure 1** illustrates the transition of the ductile-to-brittle behaviour for structural steel.

To compute the failure behaviour of structures at cold (sub-zero) temperatures (or higher than the ductile-to-brittle fracture transition temperatures), constitutive equations of materials have been proposed in the literature [12–15]. It is recognised that most of previous studies are associated with predominantly ductile behaviour or at least with partial ductility, but studies applicable to entirely brittle fracture at cryogenic condition are lacking. It is also recognised that the approaches using the constitutive equations are not always practical for the ultimate strength analysis of supersized structures because they are too complex to apply for the problem.

This chapter presents a method for computing the ultimate compressive strength of steel stiffened-plate structures by nonlinear finite element method (NLFEM) using the multi-physics software package LS-DYNA implicit code. Mechanical properties of high-strength steel with grade AH32 used for fabricating the tested structure were obtained from tension and compression tests at low temperatures and cryogenic condition [7, 8], and a phenomenological relation of engineering stress versus engineering strain of the material was formulated. The material model is implemented into the LS-DYNA implicit code. To demonstrate the validity of the computational model, the NLFEM is compared to experimental results from a full-scale physical test.

2. Literature survey on structural behaviour at cold (sub-zero) temperatures

A number of studies in modelling of material behaviour for structural steels at cold (sub-zero) temperatures are available in the literature. Most of the studies dealt

with predominantly ductile behaviour of materials with the focus on how crack initiates in association with ductile fracture. Ehlers and Varsta [16] and Ehlers [17] derived the true stress versus true strain relation of ordinary steel. The effects of stress triaxiality on ductile fracture have been one of research topics [18–24]. The works of the Choung group have provided useful insights for ductile fracture behaviour of structural steels [14, 25–32].

It is recognised that structural steel behaviour is predominantly ductile at temperatures higher than the temperature of the ductile-to-brittle fracture transition, as shown in **Figure 1**. As the temperature decreases approaching cryogenic condition, the material behaves predominantly in a brittle manner with partial or no ductility [33–40]. Majzoobi et al. [41] observed that the ductile-to-brittle fracture transition of carbon steel occurs at about -80°C, and the material behaviour becomes entirely brittle at -196°C.

Although there are considerable uncertainties associated with the ductile-to-brittle fracture transition temperature (DBTT), a number of evidences for brittle fracture behaviour of steel structures at cryogenic condition have been seen in the literature, depending on the type of materials and loading conditions (e.g., quasi-static or impact), among other factors. Crushing testing of steel tubes under quasi-static loads at -60°C [42, 43] showed ductile fracture, as shown in **Figure 2**. Dropped-object impact testing of steel stiffened plate panels at -60°C [44] showed brittle fracture, as shown in **Figure 3**. Full-scale collapse testing of a steel stiffened-plate structure under axial-compressive loading showed that the ultimate strength was reached by a trigger of brittle fracture [1], as shown in **Figures 4** and **5**. At room temperature, the structures reached the ultimate strength by flexural-torsional buckling [1], but brittle fracture triggered the global failure at cryogenic conditions [7].

Here, an attempt is made to develop new fracture criteria based on the hypothesis that crack initiates if an equivalent stress exceeds a critical value, to model the fracture phenomenon of high-strength steel (AH32) under cryogenic conditions. Existing material models for the fracture analysis is first reviewed.

2.1 Maximum principal stress based fracture criterion

The maximum principal stress-based fracture criterion is the simplest among all fracture criteria. It is useful to predict fracture behaviour of brittle materials under predominantly tensile loads. In this criterion, brittle fracture is expected to occur when the largest principal normal stress reaches the ultimate tensile strength (σ_T) of the material, which is usually obtained from tension tests of coupon specimens. The maximum principal stress-based fracture criterion is expressed as follows:

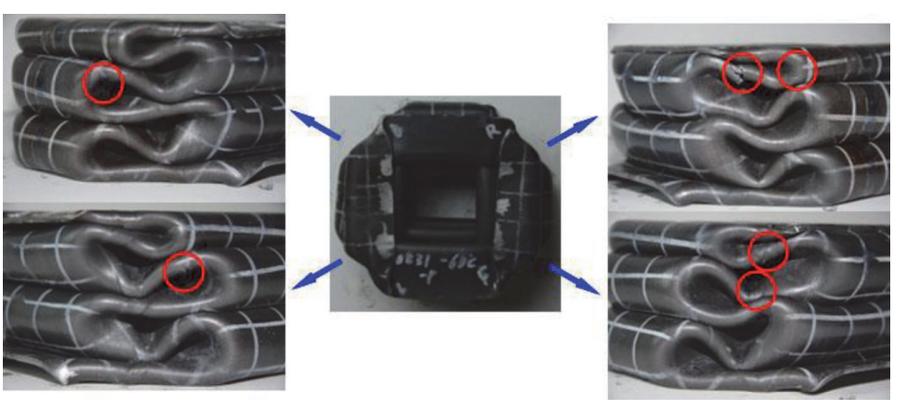

Figure 2.
Ductile fracture of a square tube under quasi-static crushing loads at -60°C [42].

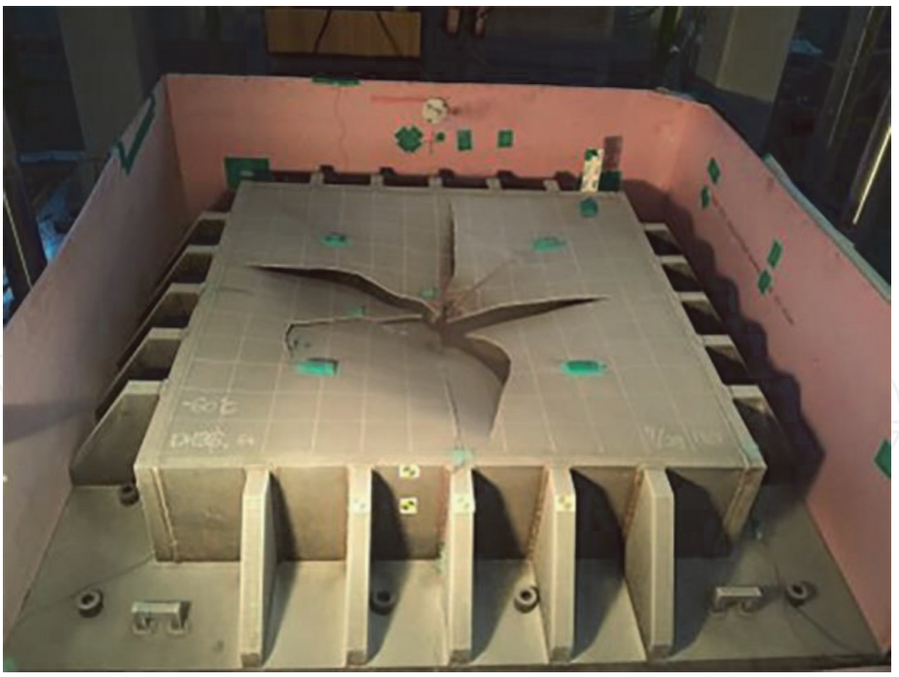

Figure 3.
Brittle fracture of a steel stiffened-panel under dropped-object impact at -60°C [44].

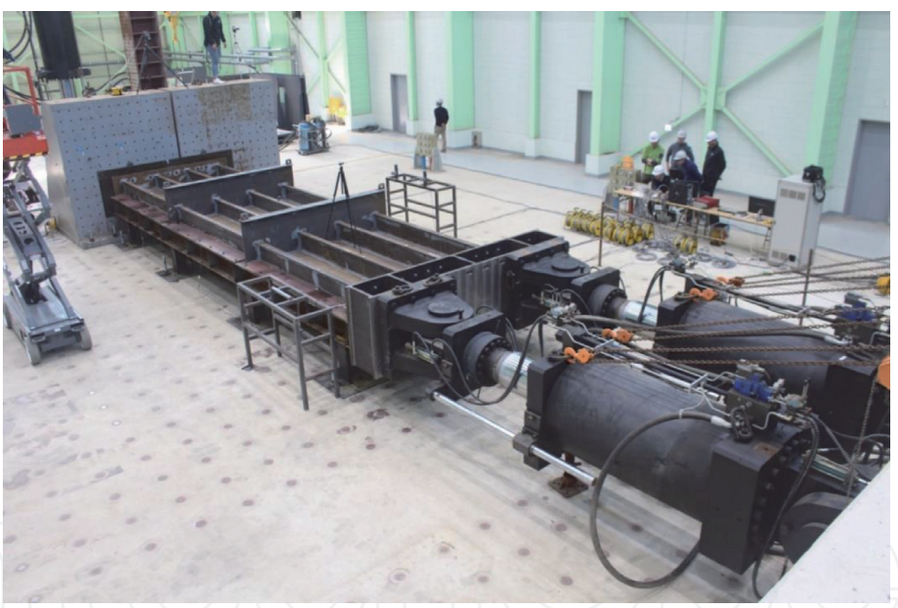

Figure 4.
The axial-compressive collapse test set-up of a full-scale steel stiffened plate structure [1, 7, 8].

$$Max.(|\sigma_1|, |\sigma_2|, |\sigma_3|) = \sigma_T \quad (1)$$

where σ_1, σ_2 and σ_3 are the principal stress components.

2.2 Coulomb-Mohr fracture criterion

The Coulomb-Mohr fracture criterion gives reasonably accurate predictions of fracture in brittle materials for which the compressive strength far exceeds the tensile strength, e.g., concrete or cast iron [45]. It is presumed that fracture occurs in a certain stress plane of material when a critical combination of normal stress and shear stress acts on the plane. The linear relation of the combination of critical stresses is given by:

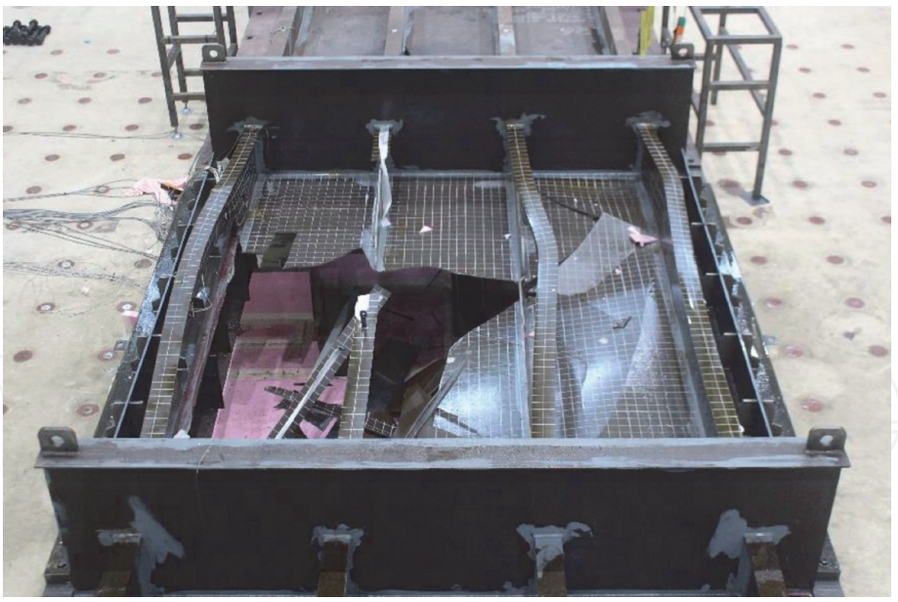

Figure 5.
Brittle fracture of a full-scale steel stiffened plate structure under axial-compressive loads at -160°C [7].

$$|\tau| + \mu\sigma = \tau_i \tag{2}$$

where τ is the shear stress, σ is the normal stress, μ and τ_i are constants for a given material.

2.3 Johnson-Holmquist fracture criterion

The Johnson-Holmquist fracture criterion [46] is useful for modelling brittle materials, e.g., ceramic and glass, over a range of strain rates. It is one of the most widely used models in dealing with the ballistic impact on ceramics, which is expressible as follows:

$$\sigma^* = \sigma_i^* - D\left(\sigma_i^* - \sigma_f^*\right) \tag{3}$$

where σ_i^* is the uniaxial failure strength of intact material, see Eq. (4), σ_f^* is the uniaxial failure strength of completely fractured material, see Eq. (5), and D is a damage accumulation variable, see Eq. (6).

$$\sigma_i^* = A(p^* + T^*)^n\left[1 + C\ln\left(\frac{d\varepsilon_p}{dt}\right)\right] \tag{4}$$

$$\sigma_f^* = B(p^*)^m\left[1 + C\ln\left(\frac{d\varepsilon_p}{dt}\right)\right] \tag{5}$$

$$\frac{dD}{dt} = \frac{1}{\varepsilon_f}\frac{d\varepsilon_p}{dt} \tag{6}$$

where A, B, C, m, n are material constants, t is time, ε_p is the inelastic strain, and ε_f is the plastic strain to fracture. The asterisk indicates a normalised quantity, where the quantities of each variable are defined as follows:

$$\sigma^* = \frac{\sigma}{\sigma_{hel}}, p^* = \frac{p}{\sigma_{hel}}, T^* = \frac{T}{p_{hel}} \tag{7}$$

where σ^* and p^* are the stresses normalised by the stress at the Hugoniot elastic limit, and T^* is the tensile hydrostatic pressure normalised by the pressure at the Hugoniot elastic limit.

The Johnson-Holmquist damage model was modified by Deshpande and Evans [47] and Bhat et al. [48], where it is considered that the propagation of an initial crack is a function of the stress state, the fracture toughness and the flaw characteristics.

3. Proposed fracture criteria

The yield and ultimate tensile strengths of structural steels tend to increase with a decrease in the temperature [49], and subsequently the maximum load-carrying capacity (ultimate strength) of steel structures at cold temperatures is greater than that at room temperature [43, 50]. **Figure 6** shows a schematic of ductile and brittle failure behaviour, where the brittle fracture-induced ultimate strength P_{u2} at cryogenic condition is greater than the ductile collapse-induced P_{u1} at room temperature. However, the post-ultimate strength behaviour becomes very unstable if brittle fracture triggers the structural collapse at cryogenic condition. In this case, the strain energy absorption capability of structures can be more useful than the ultimate strength itself in terms of the structural safety assessment as it is obtained by integrating the area below the load–displacement curve until or after the ultimate strength is reached. The absorbed energy E_3 at cryogenic condition can be smaller than E_1 or E_2 at room temperature or a temperature higher than the DBTT (ductile-to-brittle fracture transition temperature). For this purpose, the entire

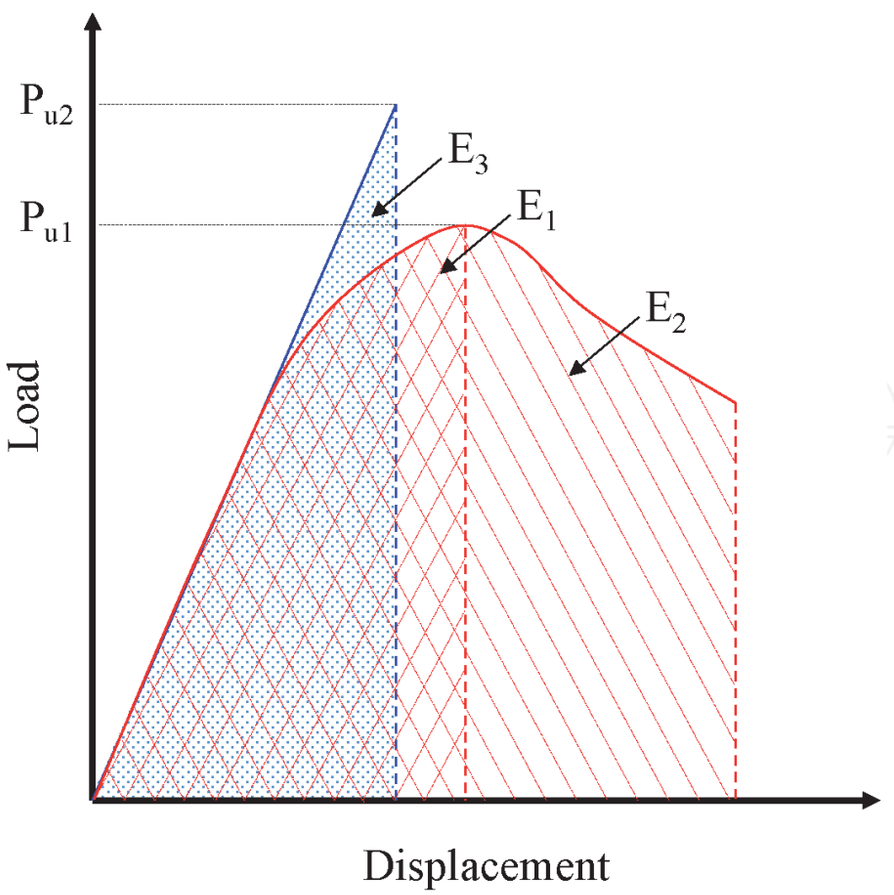

Figure 6.
Ultimate strength and post-ultimate strength behaviour at room temperature (or a temperature higher than the DBTT) versus cryogenic condition.

behaviour of structural collapse involving brittle fracture at cryogenic condition must be quantified efficiently and accurately.

3.1 Fracture criteria

A practical model is proposed for carbon steels which can be used for the ultimate strength analysis triggered by brittle fracture at cryogenic condition or in the region of ductile-to-brittle fracture transition. An elastic-perfectly plastic material model without the strain-hardening effect is used similar to a typical application at room temperature (20°C). However, the material behaviour in compression is different at low (sub-zero) temperatures or cryogenic condition from that in tension as the Bauschinger effect plays a role. However, the Bauschinger effect is usually neglected at room temperature with $\sigma_{YC} = \sigma_{YT}$, $\varepsilon_{Yc} = \varepsilon_{Yt}$ and $\varepsilon_{fc} = \varepsilon_{ft}$.

In the present model, it is hypothesised that brittle fracture occurs if the equivalent stress (σ_{eq}) reaches a fracture stress which is defined as the yield strength of material at the corresponding temperature, which can be expressed as follows:

(1) In tension:

$$\sigma_{eq} \geq \sigma_{FT} \text{ with } \sigma_{FT} = \gamma_t \sigma_{YT} \tag{8}$$

(2) In compression:

$$\sigma_{eq} \geq \sigma_{FC} \text{ with } \sigma_{FC} = \gamma_c \sigma_{YC} \tag{9}$$

where σ_{eq} is the equivalent stress, σ_{FT} and σ_{YT} are the fracture or yield stresses in tension at cryogenic condition or in the region of ductile-to-brittle fracture transition (which depends on types of materials), σ_{FC} and σ_{YC} are the fracture or yield stresses in compression at cryogenic condition or in the region of ductile-to-brittle fracture transition, γ_t and γ_c are test constants for a given steel in tension or compression, which may depend on various sources of parameters including chemical composition (grade), temperature and strain rate.

In Eqs. (6) and (7), σ_{eq} can be calculated as a function of principal stresses by the von Mises stress [51] as follows:

$$\sigma_{eq} = \frac{1}{\sqrt{2}} \sqrt{(\sigma_1 - \sigma_2)^2 + (\sigma_2 - \sigma_3)^2 + (\sigma_3 - \sigma_1)^2} \tag{10}$$

For plane stress state, σ_{eq} can be simplified as follows:

$$\sigma_{eq} = \frac{1}{\sqrt{2}} \sqrt{(\sigma_1 - \sigma_2)^2 + \sigma_2{}^2 + \sigma_1)^2} \tag{11}$$

3.2 Formulation of the engineering stress-engineering strain relations

The relations of the engineering stress versus engineering strain can be formulated following the fracture criterion defined in Section 3.1. If the steel temperature, T_s, is above the ductile-to-brittle fracture transition temperature (DBTT), i.e., $T_s >$ DBTT, the material behaves according to the ductile region. In this case, the stress–strain relation in tension is expressed as follows:

$$\sigma = \begin{cases} E\varepsilon \text{ for } \sigma < \sigma_{YT} \\ \sigma_{YT} \text{ for } \sigma = \sigma_{YT} \text{ or } \varepsilon = \varepsilon_{Yt} \\ 0 \text{ for } \varepsilon \geq \varepsilon_{ft} \end{cases} \tag{12}$$

where σ is the engineering stress, ε is the engineering strain, E is the elastic modulus, ε_{Yt} is the yield strain in tension, and ε_{ft} is the fracture strain in compression. **Figure 7** shows a schematic view of the proposed model of the engineering stress-engineering stress relation with full or partial ductility at room temperature or low temperatures.

In compression, the following equation similar to Eq. (13) is obtained.

$$\sigma = \begin{cases} E\varepsilon \; for \; \sigma < \sigma_{YC} \\ \sigma_{YC} \; for \; \sigma = \sigma_{YC} \; or \; \varepsilon = \varepsilon_{Yc} \\ 0 \quad for \; \varepsilon \geq \varepsilon_{fc} \end{cases} \tag{13}$$

where ε_{Yt} is the yield strain in tension and ε_{fc} is the fracture strain in compression.

If $T_s \leq$ DBTT or the steel temperature is lower than DBTT, the material behaves according to the brittle region. In this case, the stress–strain relation in tension is expressed as follows:

$$\sigma = \begin{cases} E\varepsilon & for \; \sigma < \sigma_{FT} \\ 0 & for \; \sigma \geq \sigma_{FT} \end{cases} \tag{14}$$

In compression, a similar equation to Eq. (14) is obtained as follows:

$$\sigma = \begin{cases} E\varepsilon & for \; \sigma < \sigma_{FC} \\ 0 & for \; \sigma \geq \sigma_{FC} \end{cases} \tag{15}$$

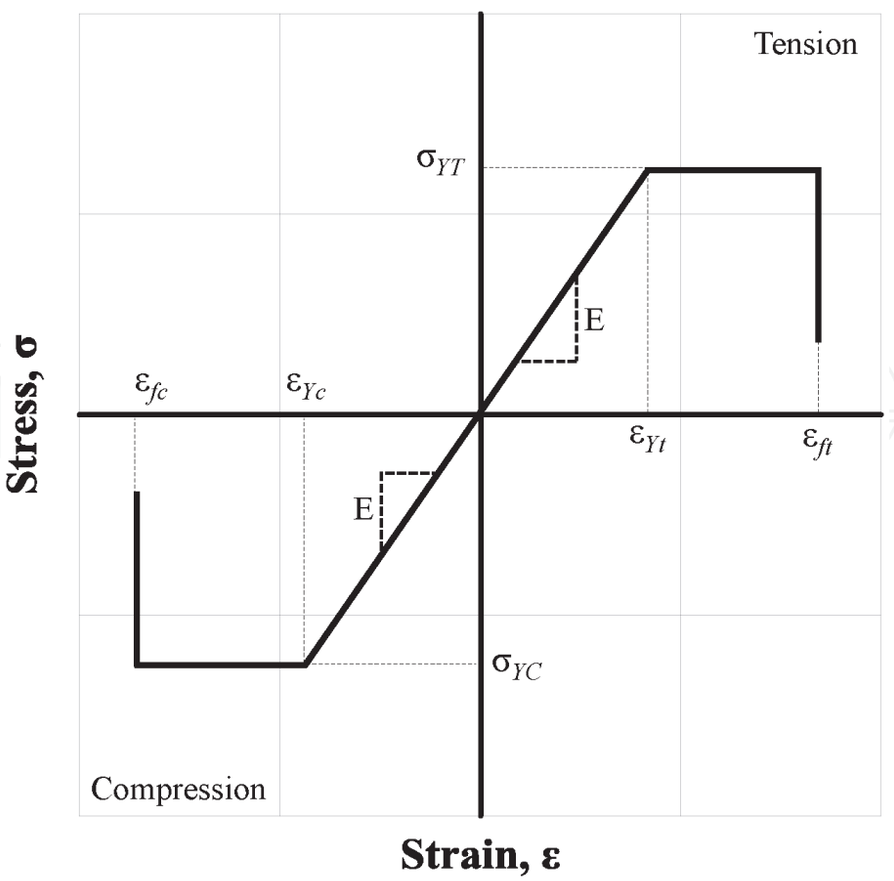

Figure 7.
Proposed model of the engineering stress-engineering stress relation with full or partial ductility at room temperature or sub-zero temperatures.

In the region of entire brittle fracture, i.e., with $T_s \leq$ DBTT, **Figure 7** can be redrawn as shown in **Figure 8** when elongation can be neglected after reaching the yield stress in tension or compression as the material exhibits brittle fracture immediately.

4. Nonlinear finite element method modelling

The proposed material model is implemented into the LS-DYNA implicit solver with 4-node shell elements (element formulation 16) for the ultimate compressive strength analysis of a structure tested at cryogenic condition as shown in **Figures 4** and **5** [7]. **Table 1** with **Figure 9** shows the dimensions of the tested structure. The nonlinear ultimate compressive strength analysis is simulated in a quasi-static analysis using the LS-DYNA implicit solver. The 4-node shell elements are used to model plating, stiffeners and transverse frames. In order to ensure sufficient resolution in the mesh size, a convergence study was performed by varying the element size following a typical approach as described in Paik [4]. The resulting convergence study provided the element size of 40 mm × 40 mm which was chosen to obtain sufficiently accurate results while minimising the computational cost. The thermal shrinkage effects for steel at low temperatures were not considered. **Figure 10** shows the FE model of the tested structure. **Figure 11** shows the loading and boundary conditions which were modelled as much as close to the tested structure, where unloaded edges were kept straight and loaded edges were entirely fixed.

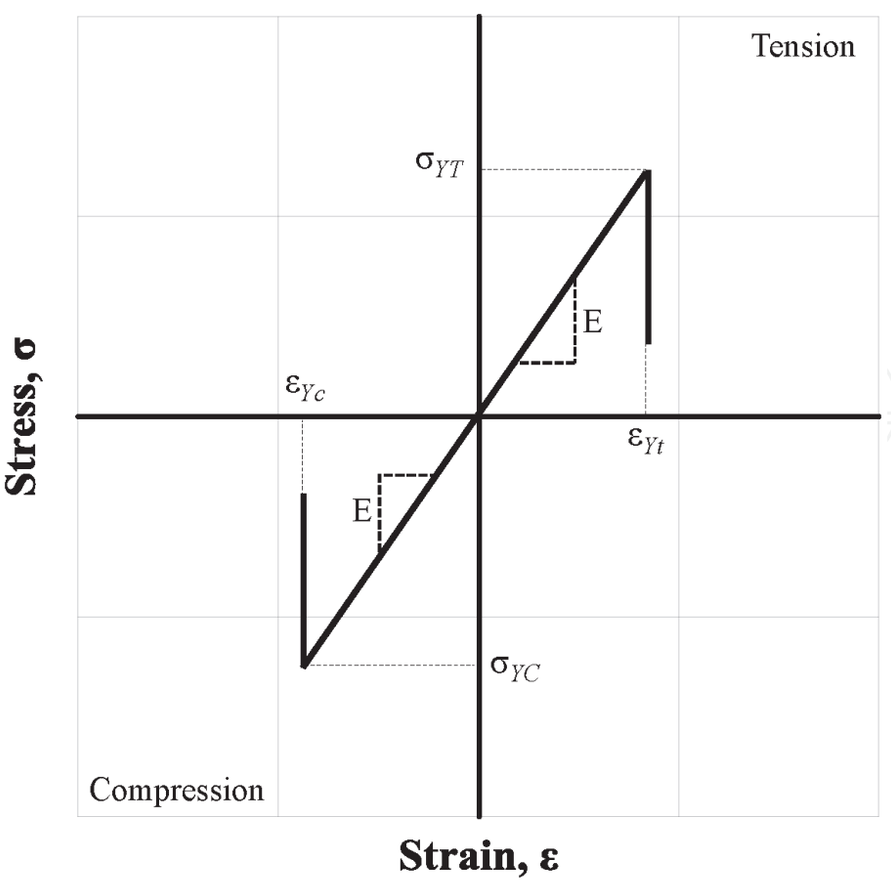

Figure 8.
Proposed model of the engineering stress-engineering strain relation without ductility or entire brittle behaviour below the ductile-to-brittle transition temperature or at cryogenic condition.

Material	AH32 high-strength steel
Spacing between transverse frames (a)	3150 mm
Spacing between longitudinal stiffeners (b)	720 mm
Plating thickness (t)	10 mm
Longitudinal stiffener (middle bay)	290 × 90 × 10/10 (T) (mm)
Longitudinal stiffener (side bays)	290 × 90 × 20/10 (T) (mm)
Transverse frame	665 × 150 × 10/10 (T) (mm)

Table 1.
Dimensions of the tested structure.

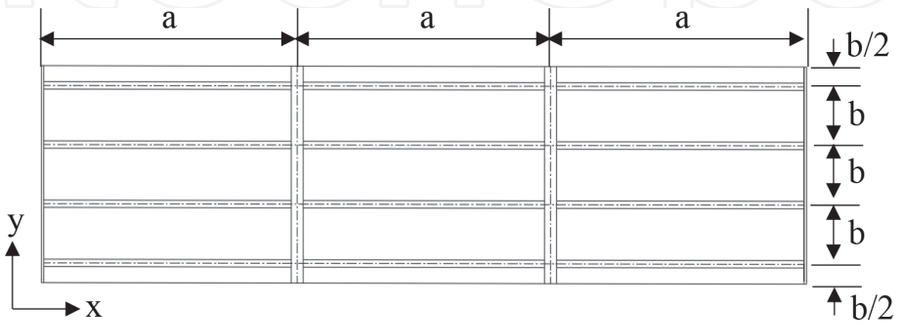

Figure 9.
Nomenclature of the scantlings for the tested structure.

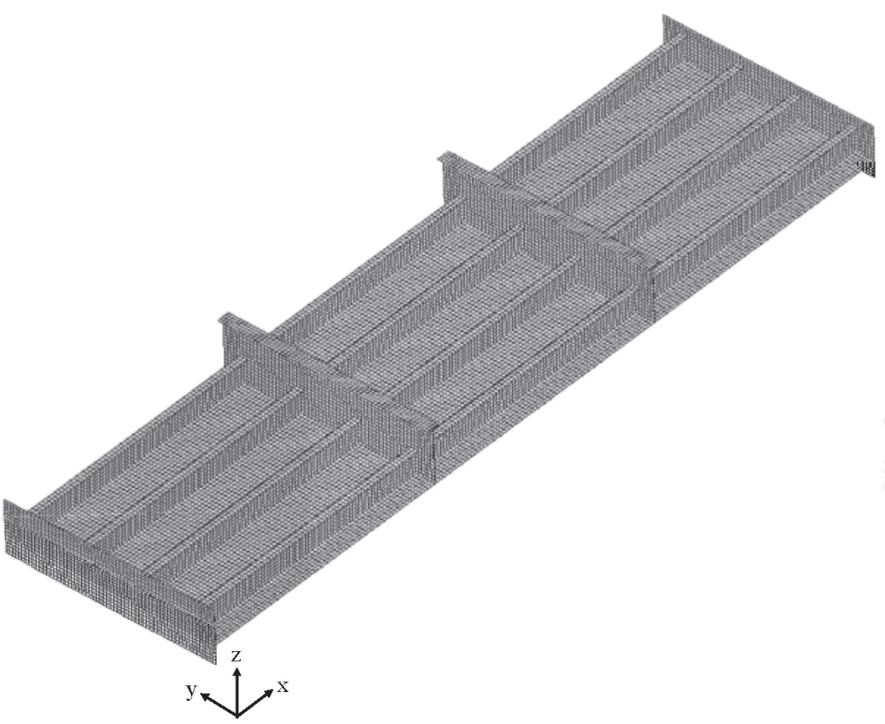

Figure 10.
Finite element mesh model of the tested structure.

Only the middle bay of the tested structure was exposed to the cryogenic condition as shown in **Figure 12**. **Table 2** summarises the measured data of steel temperatures during the collapse testing. For details of **Table 2**, see Paik et al. [7].

In room temperature, the mechanical properties of steel in compression are typically defined in the same manner as in tension without considering. However,

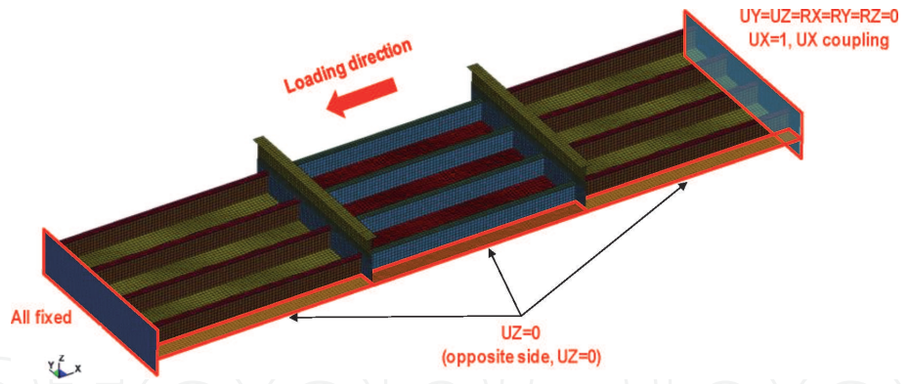

Figure 11.
The loading and boundary conditions applied to the FE model.

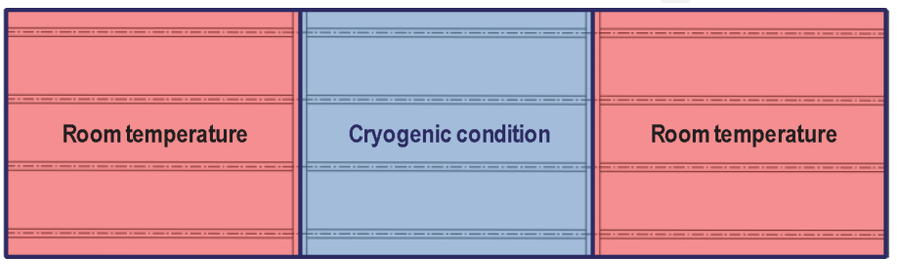

Figure 12.
Middle bay of the structure exposed to cryogenic condition.

Part	Highest temperature (°C)	Lowest temperature (°C)	Average temperature (°C)
Plating	−147.1	−175.4	−161.6
Web of longitudinal stiffener	−72.1	−167.2	−128.8
Flange of longitudinal stiffener	−58.8	−99.1	−79.3

Table 2.
Measured steel temperatures of the tested structure [7].

the Bauschinger effect cannot be neglected at low (sub-zero) temperatures and cryogenic condition [3, 10, 11]. To define the mechanical properties of AH32 steel at different temperatures (20°C, −80°C, −130°C and − 160°C), material tests in tension and compression were conducted. Details of these test data are presented in separate papers [7, 8]. **Tables 3** and **4** summarize the test data for the mechanical properties of the AH32 steel. It is found that the yield stress of steel in tension or compression increases as the temperature decreases, while the fracture strain in tension decreases with decrease in the temperature. The elastic modulus of steel

Parameter	At 20°C	At −80°C	At −130°C	At −160°C
Elastic modulus, E (GPa)	205.8	205.8	205.8	205.8
Yield stress, σ_{YT} (MPa)	358.0	433.4	546.7	672.9
Fracture strain, ε_{ft} (−)	0.376	0.430	0.409	0.336
Poisson's ratio (−)	0.3	0.3	0.3	0.3

Table 3.
Mechanical properties of AH32 steel at room and low temperatures in tension [7, 8].

Parameter	At 20°C	At −80°C	At −130°C	At −160°C
Elastic modulus, E (GPa)	205.8	205.8	205.8	205.8
Yield stress, σ_{YC} (MPa)	359.6	382.0	387.2	411.5
Poisson's ratio (−)	0.3	0.3	0.3	0.3

Table 4.
Mechanical properties of AH32 steel at room and low temperatures in compression [7, 8].

remains unchanged regardless of sub-zero temperatures. This chapter focuses on the ultimate strength of steel structures under monotonically applied compressive loads, but fatigue crack resistance at sub-zero temperatures must be associated with microstructural characteristics which are closely related to low-temperature impact toughness of steel [52, 53].

In the present case study, an elastic-perfectly plastic material model was applied without considering the strain-hardening effect. To implement the material model, *MAT_PLASTICITY_COMPRESSION_TENSION, MAT124 in LS-DYNA was used as it is an isotropic elastic–plastic material which can distinguish material behaviour in tension and compression. The von Mises yield criterion was applied using MAT124. Tension or compression was determined by the sign of the mean stress (hydrostatic stress). A positive sign which means a negative pressure is indicative of tension, or a negative sign is indicative of compression. The mean stress, σ_{mean} can be expressed as follows:

$$\sigma_{mean} = \frac{\sigma_x + \sigma_y + \sigma_z}{3} \tag{16}$$

where σ_x, σ_y and σ_z are the stress components in the x, y and z directions, respectively.

Majzoobi et al. [41] observed that the ductile-brittle transition of steel occurs at −80°C, and the material behaviour of steel is completely brittle at −196°C. With **Figure 12** and **Table 2**, the average steel temperatures of plating and web of stiffeners in the middle bay of the tested structure were −160°C and −130°C, respectively. Therefore, the plating and web of stiffeners in the middle bay of the tested structure were modelled using the engineering stress-engineering stress relation of Eqs. (12) and (13). The rest of structural members in ductile region (above −80°C) were modelled using the engineering stress-engineering stress relation of Eqs. (12) and (13). See Paik et al. [7] for details.

Three types of fabrication-related initial deformations are considered as shown in **Figure 13**. The measurement data of welding-induced initial deformations for the tested structure [54] as shown in **Figure 14** was directly applied to the FE model.

The initial deformations of the tested structure were formulated so as to make easier implementation into the FE model as shown in **Figure 15**.

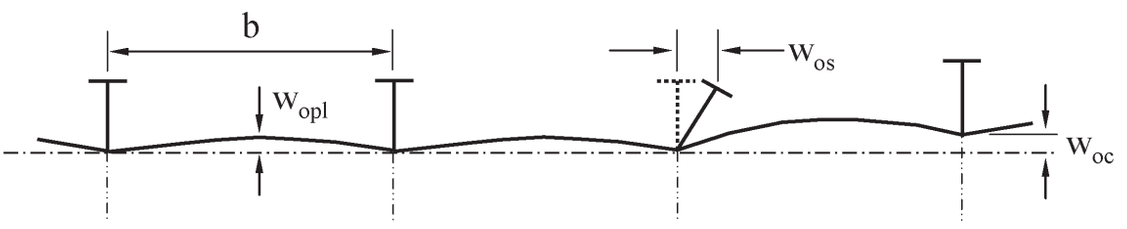

Figure 13.
Three types of welding-induced initial deformations in a stiffened plate structure.

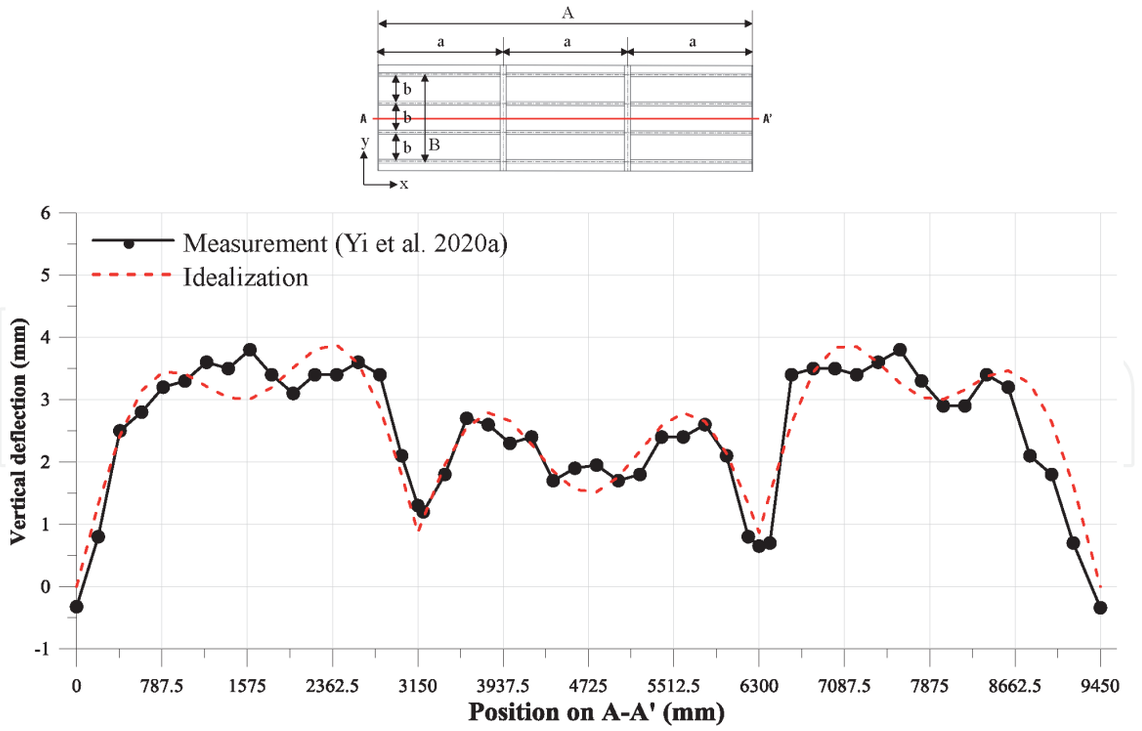

Figure 14.
Measured and idealised deformations of the tested structure due to fabrication by welding.

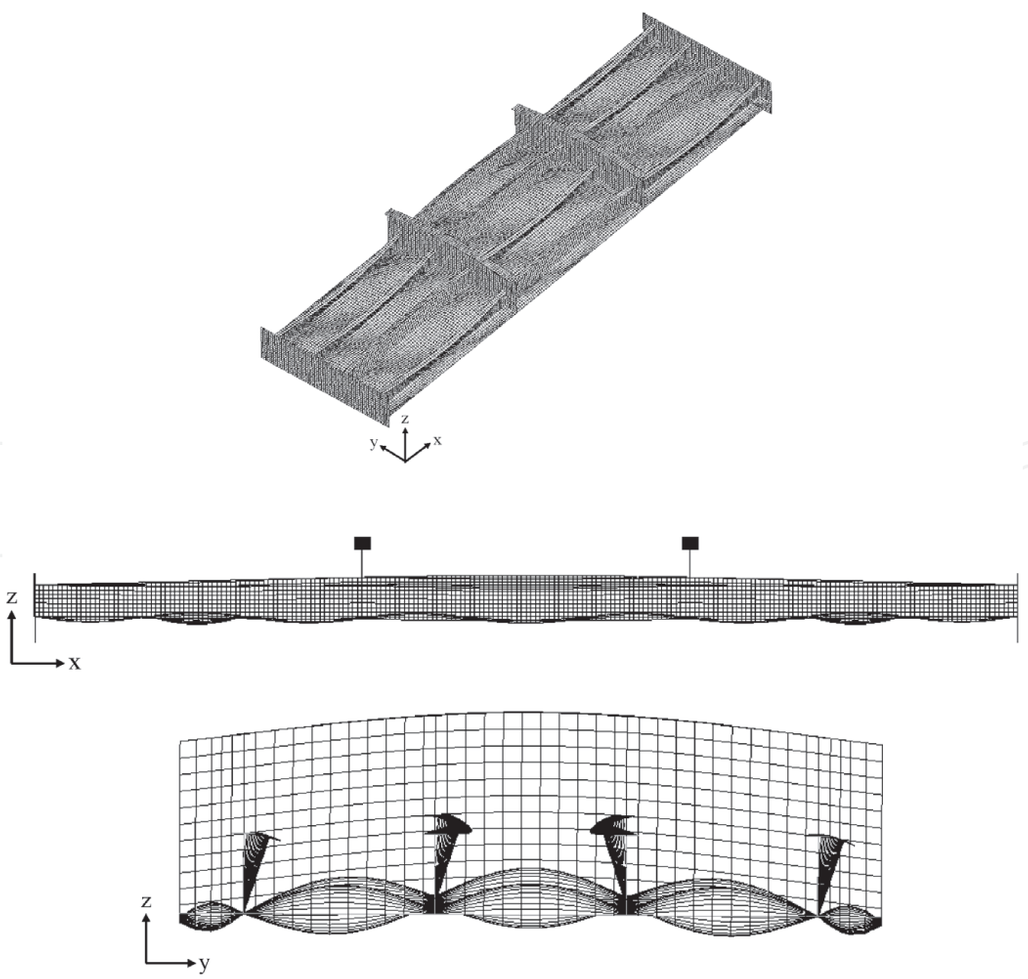

Figure 15.
Welding-induced initial deformations applied to the FE model (with an amplification factor of 100 for plating and column-type, and 20 for sideways initial deformations).

Initial deflection of plating:

$$w_{opl} = w^{*}_{opl} + w^{**}_{opl} \tag{17}$$

$$w^{*}_{opl} = w_{o\max} \sin\left(\frac{m\pi x}{a}\right)\left|\sin\left(\frac{n\pi y}{b}\right)\right| \text{ with } m = 1,\ n = 1,$$

$$w_{o\max} = \begin{cases} 3.5 \ \ for\ 0 \le x \le a, 2a \le x \le 3a \\ 1.5 \ \ for\ a \le x \le 2a \end{cases} \tag{18}$$

$$w^{**}_{opl} = w_{o\max} \sin\left(\frac{m\pi x}{a}\right)\left|\sin\left(\frac{n\pi y}{b}\right)\right| \text{ with } w_{o\max} = 1.0,\ m = 3,\ n = 1 \tag{19}$$

Column-type initial deformation of stiffener:

$$w_{oc} = w_{oc\max} \sin\left(\frac{m\pi x}{A}\right) \sin\left(\frac{n\pi y}{B}\right) \text{ with } w_{oc\max} = 1.0,\ m = 1,\ n = 1 \tag{20}$$

Sideways initial deformation of stiffener:

$$w_{os} = w_{os\max}\left(\frac{z}{h_w}\right) \sin\left(\frac{\pi x}{a}\right) \text{ with } w_{os\max} = 0.000133a \tag{21}$$

where z is the coordinate in the direction of stiffener web height, and h_w is the stiffener web height.

Biaxial residual stresses developed in the plating of the tested structure between the support members because the welding was conducted in both the longitudinal and the transverse directions to attach the longitudinal stiffeners and the transverse frames. Measurement data of the fabrication-induced residual stresses in the tested structure [55] was also directly applied to the FE model although the biaxial residual stress distributions were idealised as shown in **Figure 16** with the measurement data indicated in **Table 5**.

Stress concentration in structural details or fillet weld toe locations happens due to geometrical discontinuity, and it is a critical factor that must be considered for

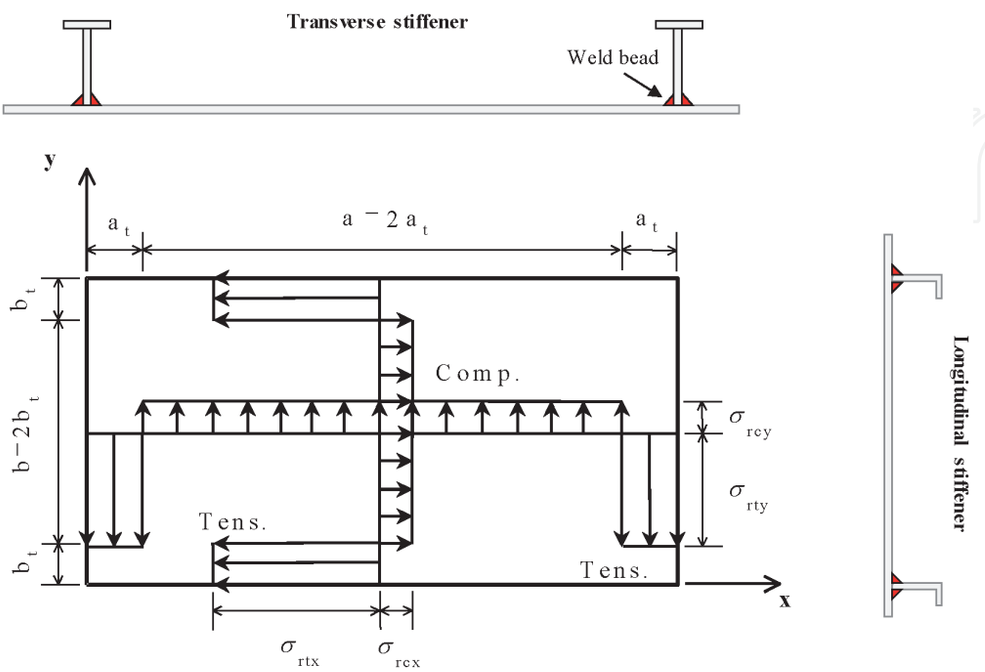

Figure 16.
Idealised distribution of biaxial residual stresses in plating of the tested structure.

	Transverse direction			Longitudinal direction	
	Simplified model	**Smith average level model**		**Simplified model**	**Smith average level model**
b_t	39.61 mm	56.80 mm	a_t	51.47 mm	64.70 mm
σ_{rcx}	$-0.110\ \sigma_{YT}$	$-0.150\ \sigma_{YT}$	σ_{rcy}	$-0.030\ \sigma_{YT}$	$-0.034\ \sigma_{YT}$
σ_{rtx}	$+0.90\ \sigma_{YT}$	$+0.80\ \sigma_{YT}$	σ_{rty}	$+0.90\ \sigma_{YT}$	$+0.80\ \sigma_{YT}$

Table 5.
Measured data of the biaxial residual stresses in the plating of the tested structure.

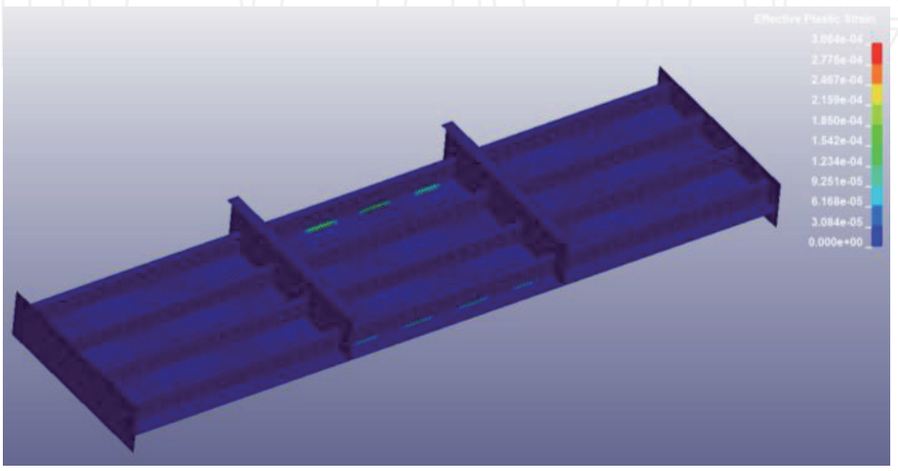

Figure 17.
Effective plastic strain (−) distribution in FE analysis on ultimate compressive strength of stiffened plate structure.

fatigue limit state analysis [3, 56]. **Figure 17** shows an example of the effective plastic strain distribution which was obtained from the FE analysis of the ultimate compressive strength of the tested structure. It is obvious from **Figure 17** that the effective plastic strain is comparatively large along the weld lines between plating and stiffeners. For the ultimate strength analysis in ductile region, e.g., at room temperature, the stress concentration at the fillet weld toes is usually ignored.

For brittle fracture analysis at sub-zero or cryogenic condition, however, the effects of stress concentration cannot be neglected [4, 44]. This is because the weld toes can reach the yield condition earlier, leading to local brittle fracture which can trigger the ultimate limit states at cryogenic condition. Therefore, the nonlinearity at weld toes along the fillet weld lines needs to take into account in the FE modelling.

One of approaches is to model the weld toes directly in the FE model using shell elements with specific properties of weld metal. **Figure 18** shows a schematic of

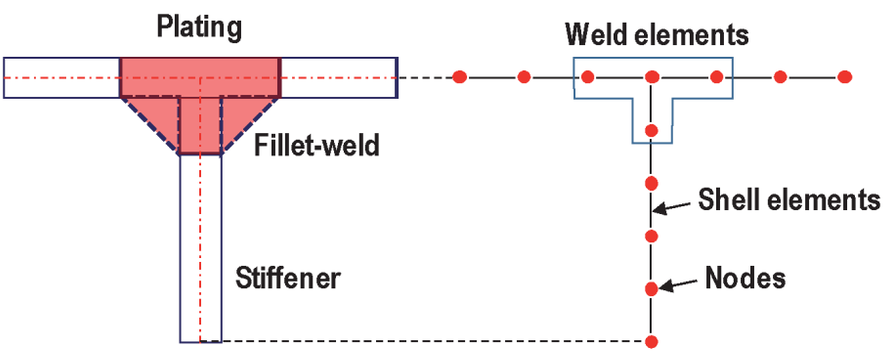

Figure 18.
Weld elements at the plate-stiffener junction.

	At 20°C	At −160°C (tension)	At −160°C (compression)
Elastic modulus, E (GPa)	268.0	268.0	268.0
Yield strength, σ_Y (MPa)	513.0	929.3	571.1
Poisson's ratio (−)	0.3	0.3	0.3

Table 6.
Mechanical properties of the weld metal with the CSF-71S at room temperature and assumed mechanical properties at −160°C.

modelling the weld toes using shell elements along the plate-stiffener junction. A similar approach was used to model weld toes by Kim et al. [44] and Nam et al. [35]. The tested structure was fabricated using flux-cored arc welding (FCAW) method and the consumable was CSF-71S, and the mechanical properties of weld metal with the CSF-71S are presented in **Table 6**. As such, the weld metal was modelled using the engineering stress-engineering strain relation of Eqs. (12) and (13). It is assumed that the yield strength of the weld metal at −160°C increases linearly in the same proportion as the steel (**Table 6**).

5. Computed results and discussion

Figure 19, **Tables 7** and **8** present the comparison results between the test and the FE analysis. The difference of ultimate strength between them is 16.6% by the ductile material model, but it becomes at most 2.3% by the brittle material model.

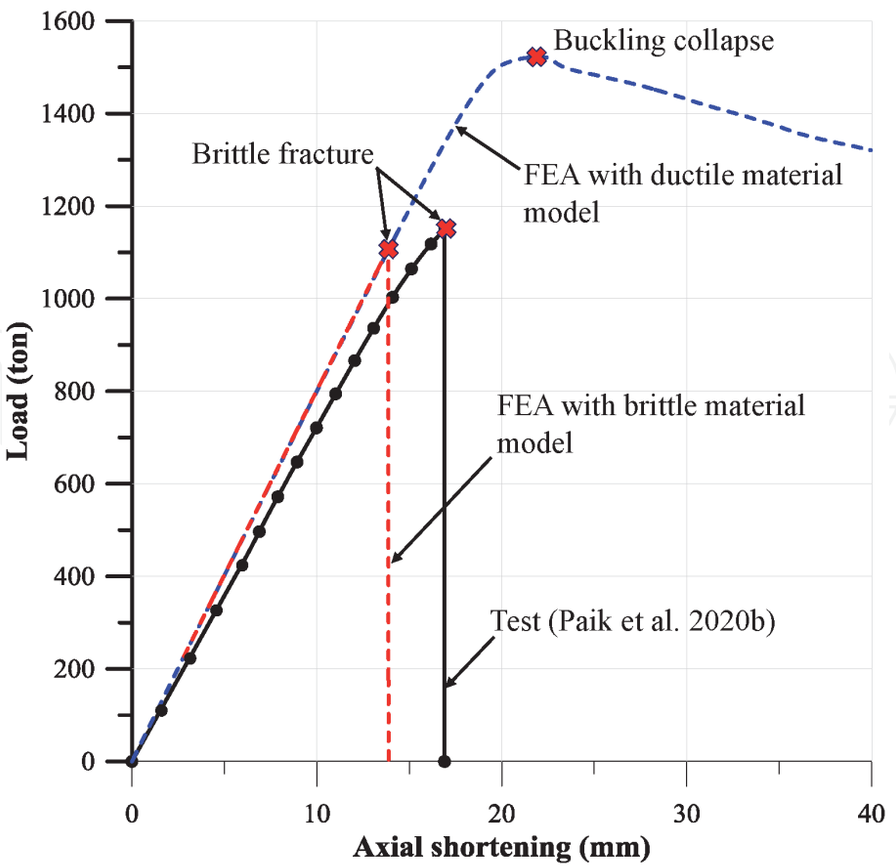

Figure 19.
Comparison of the load-axial shortening curves from the test and the FE analysis with the simplified brittle material model.

Parameter	Test [7]	FE analysis with ductile material model	Difference
Ultimate strength (ton)	1149.06	1340.14	+ 16.6%
Stiffness (ton/mm)	72.38	80.80	+ 11.6%
Axial shortening up to collapse (mm)	16.90	19.24	+ 13.8%
Strain energy up to collapse (ton·mm)	10179.96	14541.84	+ 42.8%
Local buckling	None	Occurs	—
Brittle fracture	Occurs	None	—

Table 7.
Comparison between the test and the FE analysis with the ductile material model.

Parameter	Test [7]	FE analysis with brittle material model	Difference
Ultimate strength (ton)	1149.06	1176.01	+ 2.3%
Stiffness (ton/mm)	72.38	80.82	+ 11.7%
Axial shortening up to collapse (mm)	16.90	14.75	- 12.7%
Strain energy up to collapse (ton·mm)	10179.96	8740.46	- 14.1%
Local buckling	None	None	—
Brittle fracture	Occurs	Occurs	—

Table 8.
Comparison between the test and the FE analysis with the brittle material model.

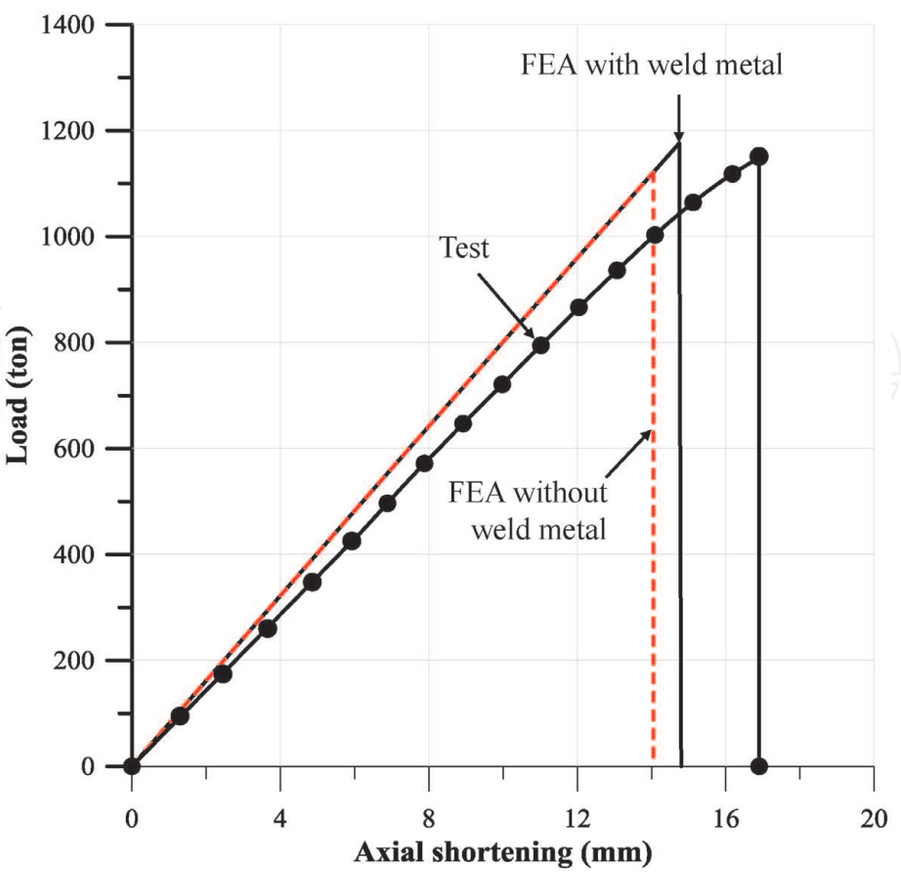

Figure 20.
Effect of weld metal on the ultimate strength behaviour.

Parameter	FEA with consideration of weld metal	FEA without consideration of weld metal	Difference
Ultimate strength (ton)	1176.01	1121.15	- 4.7%
Stiffness (ton/mm)	80.82	80.82	—
Axial shortening up to collapse (mm)	14.75	14.05	- 4.7%
Strain energy up to collapse (ton·mm)	8740.46	7908.81	- 9.5%
Local buckling	None	None	—
Brittle fracture	Occurs	Occurs	—

Table 9.
Effect of weld metal on the ultimate strength behaviour.

When only the ductile material model was applied for all structure members without considering brittle fracture, the FE analysis overestimates the ultimate strength significantly. As the yield strength of the material at cold temperature is greater than that at room temperature, the ultimate strength becomes much larger as far as brittle fracture is not allowed to happen. On the other hand, the ultimate strength obtained from the FE analysis with the brittle material model is in good agreement with the test results. **Figure 20** compares the ultimate strength behaviour with or without the weld elements along the plate-stiffener junctions. It is seen from **Figure 20** that the weld metal model increased the ultimate strength by 4.7%. This is due to the mechanical properties of weld metal which are larger than those of base metal (**Table 9**).

Figure 21 shows the deformed shape at the ultimate limit state of the tested structure obtained from the FE analysis without brittle fracture model (with only ductile material model). It is seen from **Figure 21** that the tested structure reached the ultimate limit state by tripping mode of stiffeners (without brittle fracture) which is similar to the collapse mode at room temperature [1]. However, the brittle fracture model represents brittle fracture behaviour which triggered the ultimate strength as shown in **Figure 22**, where deformed and fracture shapes of the test structures are compared between physical testing and FE analysis.

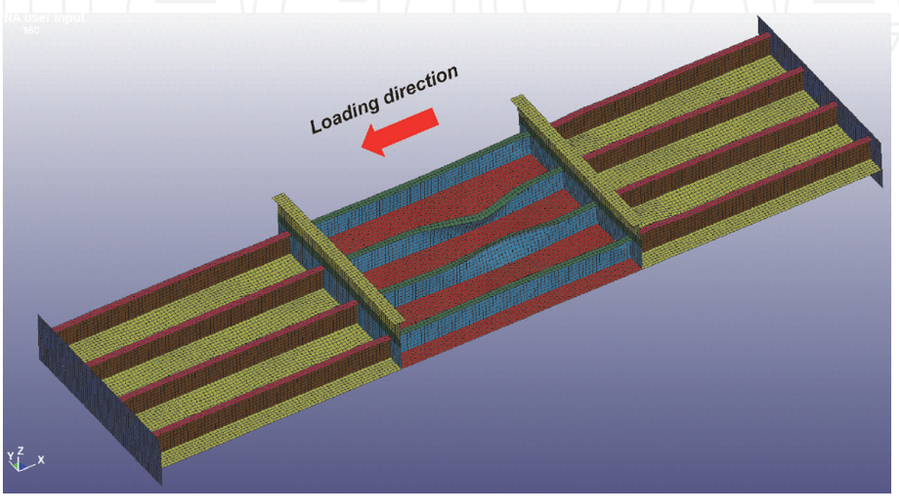

Figure 21.
Deformed shape of the tested structure at the ultimate limit state obtained from FE analysis only with ductile material model.

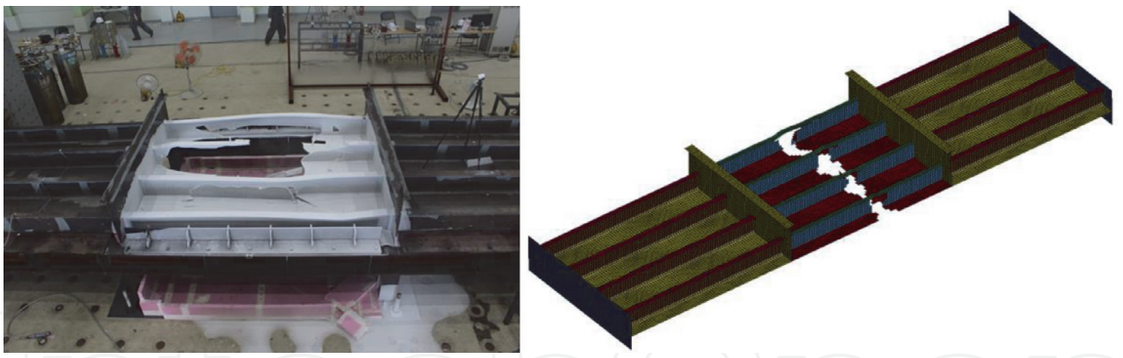

Figure 22.
Deformed shapes of the tested structure at the ultimate limit state obtained from the test and the FE analysis with brittle material model.

6. Concluding remarks

This chapter presents a practical method to compute the ultimate compressive strength of steel stiffened-plate structures at cryogenic condition which is triggered by brittle fracture. Case studies were carried out using the method, and the following conclusions were obtained together with modelling recommendations for NLFEM simulations.

1. A useful material model was formulated to analyse the brittle fracture behaviour of structural steels at cryogenic condition, where the Bauschinger effect was taken into account as the material properties in compression are distinct from those in tension

2. An elastic-perfectly plastic material model was applied without considering strain-hardening effect.

3. The developed material model was implemented into the LS-DYNA implicit code with *MAT_PLASTICITY_COMPRESSION_TENSION, MAT124.

4. Weld elements which are the same type of shell elements but with specific properties of material were introduced to model weld metal (weld toes) at the plate-stiffener junctions where stress concentrations develop. As the mechanical properties of weld metal are typically greater than those of base metal, the ultimate strength usually becomes larger with weld elements at weld toes.

5. Comparisons were made between the test results and the FE computations on a full-scale steel stiffened-plate structure at cryogenic condition. It is confirmed that the nonlinear FE analysis with the proposed material model, and the weld element model, gives a reasonably good solution of the ultimate compressive strength behaviour for steel stiffened plate structures at cryogenic condition.

Acknowledgements

This study was undertaken in the International Centre for Advanced Safety Studies, www.icass.center (the Korea Ship and Offshore Research Institute) at Pusan National University which has been a Lloyd's Register Foundation Research

Centre of Excellence since 2008. Part of the work was supported by the Swedish Research Council by the project "Fundamental research on the ultimate compressive strength of ship stiffened-plate structures at Arctic and cryogenic temperatures", contract no. 2018-06864.

Author details

Dong Hun Lee[1], Jeom Kee Paik[2,3]*, Jonas W. Ringsberg[4] and P.J. Tan[2]

1 Generic Technology Research Center, Samsung Heavy Industries Co., Ltd., Geoje, South Korea

2 Department of Mechanical Engineering, University College London, London, UK

3 The Korea Ship and Offshore Research Institute (Lloyd's Register Foundation Research Centre of Excellence), Pusan National University, Busan, South Korea

4 Department of Mechanics and Maritime Sciences, Chalmers University of Technology, Gothenburg, Sweden

*Address all correspondence to: j.paik@ucl.ac.uk

References

[1] Paik JK, Lee DH, Noh SH, Park DK, Ringsberg JW. 2020a. Full-scale collapse testing of a steel stiffened plate structure under cyclic axial-compressive loading. Structures, 26: 996–1009.

[2] Hughes OF, Paik JK. 2013. Ship structural analysis and design. Alexandria, USA: The Society of Naval Architects and Marine Engineers.

[3] Paik JK. 2018. Ultimate limit state analysis and design of plated structures, 2nd Edition. Chichester, UK: John Wiley & Sons.

[4] Paik JK. 2020. Advanced structural safety studies: with extreme conditions and accidents. Singapore: Springer.

[5] Paik JK. 2021. Ship-shaped offshore installations: design, construction, operation, healthcare and decommissioning. Cambridge University Press, Cambridge, UK.

[6] Smith CS, Davidson PC, Chapman JC, Dowling PJ. 1988. Strength and stiffness of ships' plating under in-plane compression and tension. RINA Transactions. 130: 277–296.

[7] Paik JK, Lee DH, SH, Noh, DK Park, Ringsberg JW. 2020b. Full-scale collapse testing of a steel stiffened plate structure under axial-compressive loading triggered by brittle fracture at cryogenic condition. Ships and Offshore Structures, 15(S1): S29-S45.

[8] Paik JK, Lee DH, Park DK, Ringsberg JW. 2020c. Full-scale collapse testing of a steel stiffened plate structure under axial-compressive loading at a temperature of -80°C. Ships and Offshore Structures, doi: 10.1080/17445302.2020.1791685.

[9] DNVGL (2017). Rules for classification – ships. Part 2 Materials and welding, Chapter 4 Fabrication and testing. Oslo, Norway.

[10] Brokenbrough RL, Johnston BG. 1981. USS steel design manual. United States Steel Corporation, Pittsburgh, PA, USA.

[11] Dowling NE. 2012. Mechanical behavior of materials, 4th Edition. London, UK: Pearson.

[12] Cerik BC, Choung JM. 2020. On the prediction of ductile fracture in ship structures with shell elements at low temperatures. Thin-Walled Structures. 151. doi: 10.1016/j.tws.2020.106721.

[13] Chen L, Liu W, Yu L, Cheng Y, Ren K, Sui H, Yi X, Duan H. 2020. Probabilistic and constitutive models for ductile-to-brittle transition in steels: A competition between cleavage and ductile fracture. Journal of the Mechanics and Physics of Solids. 135: 103809.

[14] Choung JM, Nam W, Lee JY. 2013. Dynamic hardening behaviors of various marine structural steels considering dependencies on strain rate and temperature. Marine Structures. 32: 49–67.

[15] Yoo SW, Lee CS, Park WS, Kim MH, Lee JM. 2011. Temperature and strain rate dependent constitutive model of TRIP steels for low-temperature applications. Computational Material Science. 50(7): 2014–2027.

[16] Ehlers S, Varsta P. 2009. Strain and stress relation for non-linear finite element simulations. Thin-Walled Structures, 47: 1203–1217.

[17] Ehlers S. 2010. Strain and stress relation until fracture for finite element simulations of a thin circular plate. Thin-Walled Structures, 48: 1–8.

[18] Bai Y, Wierzbicki T. 2008. A new model of metal plasticity and fracture

with pressure and Lode dependence. International Journal of Plasticity, 24 (6): 1071–1096.

[19] Bai Y, Wierzbicki T. 2010 Application of extended Mohr–Coulomb criterion to ductile fracture. International Journal of Fracture, 161: 1–20.

[20] Coppola T, Cortese L, Folgrarait P. 2009. The effect of stress invariants on ductile fracture limit in steels. Engineering Fracture Mechanics, 76(9): 1288–1302.

[21] Gruben G, Hopperstad OS, Børvik T. 2012. Evaluation of uncoupled ductile fracture criteria for the dual-phase steel Docol 600DL. International Journal of Mechanical Sciences, 62(1): 133–146.

[22] Lou Y, Huh H, Lim S, Pack K. 2012. New ductile fracture criterion for prediction of fracture forming limit diagrams of sheet metals. International Journal of Solids and Structures, 49(25): 3605–3615.

[23] Lou Y, Huh H. 2013. Extension of a shear-controlled ductile fracture model considering the stress triaxiality and the Lode parameter. International Journal of Solids and Structures, 50(2): 447–455.

[24] Voyiadjis GZ, Hoseini SH, Farrahi GH. 2012. Effects of stress invariants and reverse loading on ductile fracture initiation. International Journal of Solids and Structures, 49(13): 1541–1556.

[25] Cerik BC, Lee KS, Park SJ, Choung JM. 2019a. Simulation of ship collision and grounding damage using Hosford-Coulomb fracture model for shell elements. Ocean Engineering, 173: 415–432.

[26] Cerik BC, Park BJ, Park SJ, Choung JM. 2019b. Modeling, testing and calibration of ductile crack formation in grade DH36 ship plates. Marine Structures, 66: 27–43.

[27] Cerik BC, Ringsberg JW, Choung JM. 2019c. Revisiting MARSTRUCT benchmark study on side-shell collision with a combined localized necking and stress-state dependent ductile fracture. Ocean Engineering, 187. doi: 10.1016/j.oceaneng.2019.106173.

[28] Cerik BC, Park SJ, Choung JM. 2020. Use of localized necking and fracture as a failure criterion in ship collision analysis. Marine Structures, 73: doi: 10.1016/j.marstruc.2020.102787.

[29] Choung JM. 2009. Comparative studies of fracture models for marine structural steels. Ocean Engineering, 36: 1164–1174.

[30] Choung JM, Shim CS, Song HC. 2012. Estimation of failure strain of EH36 high strength marine structural steel using average stress triaxiality. Marine Structures, 29: 1–21.

[31] Noh MH, Cerik BC, Han DH, Choung JM. 2018. Lateral impact tests on FH32 grade steel stiffened plates at room and sub-zero temperatures. International Journal of Impact Engineering, 115: 36–47.

[32] Park SJ, Cerik BC, Choung JM. 2020. Comparative study on ductile fracture prediction of high-tensile strength marine structural steels. Ships and Offshore Structures, doi: 10.1080/17445302.2020.1743552.

[33] Kaminskji AA, Galatenko GV. 1999. On the temperature dependence fracture toughness in the brittle-to-ductile transition region. International Applied Mechanics. 35(4): 398–404.

[34] KSNA. 1983. Handbook for ship design. 4th Edition, The Kansai Society of Naval Architects, Osaka, Japan (in Japanese).

[35] Nam W, Hopperstad OS, Amdahl J. 2018. Modelling of the ductile-brittle fracture transition in steel structures

with large shell elements: A numerical study. Marine Structures. 62: 40–59.

[36] Nazari A, Milani AA. 2011. Ductile to brittle transition temperature of functionally graded steels with crack arrester configuration. Materials Science and Engineering: A. 528(10–11): 3854–3859.

[37] Perez-Martin MJ, Holmen JK, Thomesen S, Hopperstad OS, Børvik T. 2019. Dynamic behaviour of a high-strength structural steel at low temperatures. Journal of Dynamic Behavior of Materials. 5: 241–250.

[38] Tanguy B, Besson J, Piques R, Pineau A. 2005a. Ductile to brittle transition of an A508 steel characterized by Charpy impact test: Part I: experimental results. Engineering Fracture Mechanics. 72(1): 49–72.

[39] Tanguy B, Besson J, Piques R, Pineau A. 2005b. Ductile to brittle transition of an A508 steel characterized by Charpy impact test: Part II: modeling of the Charpy transition curve. Engineering Fracture Mechanics. 72(3): 413–434.

[40] Tong L, Niu L, Jing S, Ai L, Zhao, XL. 2018. Low temperature impact toughness of high strength structural steel. Thin-Walled Structures. 132: 410–420.

[41] Majzoobi GH, Mahmoudi AH, Moradi S. 2016. Ductile to brittle failure transition of HSLA-100 steel at high strain rates and subzero temperatures. Engineering Fracture Mechanics. 158: 179–193.

[42] Paik JK, Kim BJ, Park DK, Jang BS. 2011. On quasi-static crushing of thin-walled steel structures in cold temperature: experiment and numerical studies. International Journal of Impact Engineering, 38: 13–28.

[43] Park DK, Kim DK, Park CH, Jang BS, Kim BJ, Paik JK. 2015. On the crashworthiness of steel-plated structures in an Arctic environment: an experimental and numerical study. Journal of Offshore Mechanics and Arctic Engineering, 137: 051501–1–051501-11.

[44] Kim KJ, Lee JH, Park DK, Jung BK, Han X, Paik JK. 2016. An experimental and numerical study on nonlinear impact responses of steel-plated structures in an Arctic environment. International Journal of Impact Engineering. 93: 99–115.

[45] Juvinal RC, Marshek K. 2011. Fundamentals of machine component design, 5th Edition. Chichester, UK: John Wiley & Sons.

[46] Johnson GR, Holmquist TJ. 1994. An improved computational constitutive model for brittle materials. High-Pressure Science and Technology, American Institute of Physics.

[47] Deshpande, V. S., Evans, A. G. (2008). 'Inelastic deformation and energy dissipation in ceramics: A mechanism-based constitutive model'. Journal of Mechanics and Physics of Solids, 56(10): 3077–3100.

[48] Bhat HS, Rosakis AJ, Sammis CG. (2012). 'A micromechanics based constitutive model for brittle failure at high strain rates'. Journal of Applied Mechanics, 79(3): 031016, doi: 10.1115/1.4005897.

[49] Paik JK, Kim KJ, Lee JH, Jung BG, Kim SJ. 2017. Test database of the mechanical properties of mild, high-tensile and stainless steel and aluminium alloy associated with cold temperatures and strain rates. Ships and Offshore Structures, 12(S1): S230-S256.

[50] Ehlers S, Østby E. 2012. Increased crashworthiness due to arctic conditions–The influence of sub-zero temperature. Marine Structures. 28: 86–100.

[51] von Mises R. 1913. Mechanik der festen Körper im plastisch-deformablen Zustand. Nachrichten von der Gesellschaft der Wissenschaften zu Göttingen. Mathematisch-Physikalische Klasse. (1): 582–592.

[52] Jorge JCF, de Souza LFG, Mendes MC, Bott IS, Araújo LS, dos Santos VR, Rebello JMA, Evans GM. 2021. Microstructure characterization and its relationship with impact toughness of C-Mn and high strength low alloy steel weld metals – a review. Journal of Materials Research and Technology. 10: 471–501.

[53] Kang YJ, Park GT, Jeong SH, Lee CH. 2018. Correlation between microstructure and low-temperature impact toughness of simulated reheated zones in the multi-pass weld metal of high-strength steel. Metallurgical and Materials Transactions A, 59: 177–186.

[54] Yi MS, Lee DH, Lee HH, Paik JK. 2020. Direct measurements and numerical predictions of welding-induced initial deformations in a full-scale steel stiffened plate structure. Thin-Walled Structures, doi: 10.1016/j.tws.2020.106786.

[55] Yi MS, Noh SH, Lee DH, Seo DH, Paik JK. 2021. Direct measurements and numerical predictions and simple formula estimations of welding-induced biaxial residual stresses in a full-scale steel stiffened plate structure. Structures, 29: 2094–2105.

[56] Lotsberg I. 2016. Fatigue design of marine structures. Cambridge University Press, Cambridge, UK.